Applied Catalysis B: Environmental 266 (2020) 118630

Contents lists available at ScienceDirect

Applied Catalysis B: Environmental

journal homepage: www.elsevier.com/locate/apcatb

Hierarchically micro- and meso-porous Fe-N_4O-doped carbon as robust electrocatalyst for CO_2 reduction

Xiaoshan Wang[a], Yuanyuan Pan[a], Hui Ning[a,*], Hongmei Wang[a], Dianliang Guo[a], Wenhang Wang[a], Zhongxue Yang[a], Qingshan Zhao[a], Bingxing Zhang[b], Lirong Zheng[c], Jianling Zhang[b,*], Mingbo Wu[a,*]

[a] College of Chemical Engineering, College of New Energy, Institute of New Energy, State Key Laboratory of Heavy Oil Processing, China University of Petroleum (East China), Qingdao 266580, PR China

[b] Beijing National Laboratory for Molecular Sciences (BNLMS), CAS Key Laboratory of Colloid, Interface and Chemical Thermodynamics, CAS Research/ Education Center for Excellence in Molecular Sciences, Institute of Chemistry, Chinese Academy of Sciences, Beijing 100190, PR China

[c] Beijing Synchrotron Radiation Facility (BSRF), Institute of High Energy Physics, Chinese Academy of Sciences, Beijing 100049, PR China

ARTICLE INFO

Keywords:
CO_2electroreduction
Single atom
Iron-Nitrogen doped
Porous carbon

ABSTRACT

Electrochemical reduction of carbon dioxide (CO_2) is a potentially useful step in energy storage and greenhouse gas alleviation. Here we demonstrate for the first time a Fe-N_4O-doped nanoporous carbon as robust electrocatalyst for CO_2 reduction, where the five-coordinated Fe-N_4O structure works as catalytically active site. It exhibits a high faradaic efficiency of 96 % towards CO with partial current density of -5.4 mA cm^{-2} at low overpotential of 470 mV. First-principles density functional theory calculations reveal that the free energy barrier for *CO desorption is greatly reduced on Fe-N_4O site compared to Fe-N_4, resulting in a higher selectivity to CO for a wider electrochemical window. This work opens up new possibilities for improving the catalytic performance of metal-N-C electrocatalysts by regulating the co-ordination of metal atom.

1. Introduction

Electrochemical reduction of carbon dioxide (CRR) to valuable chemicals has become a promising route to store renewable electrical energy and mitigate greenhouse effects [1,2]. However, carbon dioxide is inert and the inherently sluggish reaction kinetics of CRR makes the development of robust electrocatalysts a highest priority currently. Among the diverse kinds of electrocatalysts for CRR [3,4], the metal-nitrogen-doped carbon (M-N-C) nanomaterials (M = Fe, Co, Ni, Cu, Zn, Mn, etc.) have been considered as the most promising catalyst for CRR due to their high activity and durability in both alkaline and acidic media [5–8].Since Fe is one of the most earth-abundant metals, it is of great significance to build highly efficient Fe-N-C catalysts for industrialized CRR [9–11]. Early in 2012, Costentin et al. found Fe-porphyrins modified by phenolic groups manifested a CO faradaic yield above 90 % through 50 million turnovers over 4 h of electrolysis at low overpotential (465 mV) with no observed degradation, where the Fe-N_4 site in the macrocycles is proved to be the active center. By incorporating Fe element atomically into nitrogen doped carbon materials, the Fe-N-C carbon materials with Fe atoms coordinated to N functionalities (Fe-N_x) were obtained with similar active sites as those in Fe-N-macrocycles for CRR [12]. For example, Strasser et al. [13] proved the intrinsic catalytic reactivity of Fe-N-C catalyst for CRR to CO can rival Au- and Ag-based catalysts. So far, tremendous of works have been carried out to investigate the catalytic performance of Fe-N-C materials towards CRR, most of which take Fe-N_4 as active sites [14,15].

However, Fe-N_4 based catalysts usually manifest a moderated catalytic performance, which is closely related to the preparation method of Fe-N-C materials. For example, Jaouen et al. [16] synthesized a Fe-N-C material by pyrolysis of Zn-based zeolitic imidazolate framework (ZIF-8), ferrous acetate, and phenanthroline, which exhibited a maximum faradaic efficiency (FE) of 91 % towards CO at an overpotential (η) of 490 mV. With different preparation methods, the reported performance of Fe-N-C catalysts manifested a maximum FE from 80 % to 90 % towards CO at a comparatively larger η in the range of 400–600 mV [17]. Daasbjerg et al. [15] tested the effect of the electrode potential on catalytic activity of Fe-N_4 electrocatalyst deposited on a glassy carbon plate for CRR in aqueous 0.5 M $KHCO_3$ solution. At various potentials between -0.97 and -0.37 V vs reversible hydrogen

* Corresponding authors.
E-mail addresses: ninghui@upc.edu.cn (H. Ning), zhangjl@iccas.ac.cn (J. Zhang), wumb@upc.edu.cn (M. Wu).

https://doi.org/10.1016/j.apcatb.2020.118630
Received 27 November 2019; Received in revised form 7 January 2020; Accepted 11 January 2020
Available online 13 January 2020

electrode (RHE), the maximum FE of CO reach 85 % at -0.47 V vs RHE with current density of -1.5 mA cm^{-2}. At more negative potentials than -0.70 V vs RHE, the current density increases to -6.0 mA cm^{-2} while the FE of CO starts decreasing to less than 60 %. Similar conditions were also found in other reports [14,18,19]. For most of Fe-N_4 active sites, it is generally agreed that the low selectivity to CRR at larger negative potentials is attributed to the strong binding of CO onto Fe atom, leading to a deceleration of CO desorption but acceleration of hydrogen electroreduction reaction (HER). Therefore, it may be a preferred option to enhance the catalytic performance of Fe-N-C catalysts by regulating the co-ordinational of Fe atom.

Recently, Wang et al. [20] synthesized a Fe-N_5 catalyst through thermal pyrolysis of hemin and melamine co-adsorbed on graphene, where N-dopant in graphene forms an additional axial nitrogen coordinated with Fe-N_4 to form new Fe-N_5 catalytic site. In a 0.1 M $KHCO_3$ solution, a high FE (~97.0 %) was achieved for the CO production at a low overpotential of 350 mV. More importantly, it has been proved the Fe-N_5 samples shows a much better electrocatalytic performance than Fe-N_4. Further DFT calculations reveal that the axial pyrrolic-nitrogen ligand of the Fe-N_5 site depletes the electron density of Fe 3d orbitals and thus reduces the Fe−CO π back-donation, responsible for the rapid desorption of CO, leading a higher selectivity towards CO production comparison with that of Fe-N_4. However, like most of the Fe-N-C materials reported, the FE of CO drops swiftly when the applied potential move to more negative region [14,21]. Apart from the active center, the catalytic performance of Fe-N-C materials is also sensitive to the carbon framework, which is critical for the mass transport and the exposure of active sites [22,23]. For example, Wang et al. reported a porous N-doped carbon membranes in which hierarchical pores is responsible for the large surface areas and the high accessibility of reactants to active sites, developing high activity and selectivity for CRR [24]. Qiu et al. synthesized a highly porous Fe doped carbon material with ZIF-8 and SiO_2 as templates by carbonization and acid leaching method, predicting the mesopores and macropores in the catalyst may be associated with the improvement in the CO selectivity during CO_2 electroreduction [11]. For now, a detailed fundamental mechanistic understanding of the CRR on Fe-N-C materials is still inadequate. Meanwhile, searching for new method and strategy to enhance the activity and selectivity of Fe-N-C catalysts remains a great challenge.

Herein, we explore a new type of Fe-N-C material with Fe-N_4O active sites, in which the oxygen atom takes the out-of-plane coordination position of Fe atom in Fe-N_4 structure. Using as electrocatalyst for CRR, a high FE of ~96 % is achieved for CO at -0.57 V vs RHE with -5.6 mA cm^{-2} and remarkable durability (> 20 h without decay). When the applied potentials are negatively shifted to -0.87 V vs RHE, the FE of CO remains higher than 80 %. Interestingly, we found the RDS of CO_2-to−CO on the Fe-N_4O site is the formation of COOH*, which is obviously different with Fe-N_4. Aside from the active site, rational designing of carbon framework structures further elevates the catalytic performance of Fe-N_4O active sites. The convenient method and new strategy will be very important for reforming the catalytic performance of M-N-C electrocatalysts.

2. Experimental section

2.1. Synthesis of Fe-N/O-doped carbon materials

For a typical procedure, 2 g magnesium oxide was added into 20 ml deionized water under constant stirring. Then, 8 mmol D-glucosamine hydrochloride, 1.6 mmol $ZnCl_2$ and 0.8 mmol $FeCl_3$ were added in turn. The resulting mixture was stirred for one hour at room temperature followed by freeze drying. After that, the obtained dried powder was collected and annealed under nitrogen atmosphere with an elevated heat rate of 5℃/min to 1000℃ and kept for two hours. The obtained power was washed thoroughly with 2 M HCl overnight at room temperature to remove any metallic or metal oxide crystallites. Finally, a black powder material was obtained after freeze drying, named Fe-N/O-C (MZ). For comparison, Fe-N/O-C (M) and Fe-N/O-C (Z) electrocatalysts were synthesized with only MgO or $ZnCl_2$ as template respectively, while keeping all other conditions unchanged.

2.2. Characterizations

The crystal structure information of samples was collected in X-ray diffraction (X'Pert PRO MPD, Holland) along with Cu Kα (λ = 0.15406 nm). To observe the surface morphology of each electrocatalysts, field emission scanning electron microscopy (FE-SEM, Hitachi S-4800, Japan) and high-resolution transmission electron microscopy (HRTEM, JEM-2100UHR, Japan) were used. High-angle annular dark field-scanning transmission electron microscopy (HAADF-STEM) measurements were performed for high-resolution images with JEM-ARM200 F (JEOL, Japan). The structural disorder of carbon frameworks was studied by the LabRAM HR Ecolution Raman spectrometer (Renishaw RM2000, Britain) with 514 nm laser. The surface area was evaluated by the Brunauer-Emmett-Teller (BET) method on the instrument of ASAP-2020 using adsorption branch. The pore size distribution was obtained by the Barrett-Joyner-Halenda method using the adsorption branch. The elemental contents were analyzed by X-ray photoelectron spectrometer (XPS, Escalab 250Xi, UK) using Al Kα radiation and 500 μm X-ray spot. The inductively coupled plasma optical emission spectroscopy (ICP-OES) was carried out on Varian 720-ES, US. X-ray absorption near edge structure (XANES) and extend X-ray absorption fine structure (XAFS) were investigated at 1W1B station in Beijing Synchrotron Radiation Facility (BSRF). All the catalysts were characterized by Fe-K edge XANES and EXAFS in transmission mode using ionization chamber. All spectra were collected in ambient conditions.

2.3. Electrochemical measurements

Electrochemical measurements were performed in a three-electrode system with two-compartment cell connected to an electrochemical workstation (CHI 760E, CH Instrument, China). The cathode and anode compartments were separated by a proton exchange membrane (Nafion 117), both of which contained 30 ml of 0.1 M $KHCO_3$ as electrolyte. The KCl-saturated Ag/AgCl and Pt net were used as the reference electrode and counter electrode, respectively. 1 mg of catalysts and 10 μL of Nafion solution (5 wt%) were dispersed in 200 μL of ethanol by sonicating for 30 min to form a homogeneous ink. The catalyst ink was painted onto a piece of carbon paper (1 cm^2, Toray TGP-H-060) and dried at atmosphere for more than 30 min to serve as working electrode. The catalyst loading was 1.0 mg cm^{-2}. The linear sweep voltammetry (LSV) was performed at 20 mV s^{-1} in CO_2-saturated 0.1 M $KHCO_3$ electrolyte (pH = 6.8) followed by a chronoamperometric measurement for 30 min. All potentials in this study were measured against the Ag/AgCl reference electrode and converted to the RHE reference scale using $E\ (vs\ RHE) = E\ (vs\ Ag/AgCl) + 0.21\ V + 0.0591 \times pH$ [25].

2.4. Analysis of products

The gas products of CRR were detected by an on-line micro gas chromatography (GC) (BFRL-3420A, China) equipped with a thermal conductivity detector (TCD) and a flame ionization detector (FID). Argon was used as the carrier gas. High purity CO_2 was purged into the 0.1 M $KHCO_3$ solution under stirring for 30 min until it was saturated, then quantification gas products were analyzed at each potential for at least 20 min during CO_2 electroreduction. The faradaic efficiencies of gas products and CO formation turnover frequency (TOF) at applied potentials were calculated by using the reported equations (see the Supporting Information) [26]. The liquid products were analyzed on a

Bruker AVANCE III 400 MHz nuclear magnetic resonance (NMR) spectrometer.

2.5. Density functional theory (DFT) calculations

The first principles calculations were carried out on the Vienna ab initio simulation package known as VASP. Perdew-Burke-Ernzerhof (PBE) functional was adopted for the electron-electron interaction, and projector augmented wave (PAW) scheme was used for describing the interaction between ions and valence electrons. An energy cutoff of 500 eV was used and a *k*-point sampling set of 2 × 2 × 1 was allowed to relax all atomic coordinates. The periodical unit cell was surrounded by the vacuum space, which was specified to be ~15 Å. Each atom in the simulated models was relaxed to the minimum in the enthalpy under force tolerance of 0.05 eV $Å^{-1}$ and conventional energy of 5.0×10^{-4} Å. In addition, a monolayer of water was considered as explicit solvation model for solvation energies calculation. All the calculations are no spin polarized calculations. Gibbs free energies for each gaseous and adsorbed species were calculated at 300 K, according to the expression: $G = E_{DFT} + E_{ZPE} - TS$ [27].

3. Results and discussion

3.1. Structural characterizations

The Fe-N/O−C materials were synthesized through a freeze-vacuum drying-calcination method, as illustrated in Fig. 1a. The SEM image (Fig. 1b) of Fe-N/O−C (MZ) clearly reveals the hierarchically micro- and meso-porous structures (around ten nanometers in diameter) with interconnected channel and thus fully accessible surfaces. TEM images (Fig. 1c) shows that the Fe-N/O−C (MZ) consists of abundant irregular open mesopores and fully interconnected structures while the curved graphitic texture with an interplanar spacing of 0.35 nm were also observed in its high-resolution TEM (HRTEM) images, as shown in Fig. S1a. The dispersing diffraction ring in selected area electron diffraction (SAED) patterns (Fig. S1b) indicates all the Fe-N/O−C materials have an amorphous carbon framework. To be specific, the evolution of homogeneity of active sites with single-atom feature and the porous carbon structure were simultaneously realized in Fe-N/O−C (MZ). Raman spectra display two characteristic peaks of G band (1600 cm^{-1}) and D band (1330 cm^{-1}) in Fig. S2, suggesting the presence of graphitic carbon in all the Fe-N/O−C materials. Noticeably, Fe-N/O−C (MZ) has the largest I_D/I_G among all the Fe-N/O−C materials as made, indicating more distortions are formed in the carbon framework. It has been proved that the structural distortions of graphene-like material help to decrease the surface energy and increase the amounts of active site like pyridinic N and Fe-N species [28]. The atomically dispersed Fe atoms in porous carbon frameworks are verified by aberration-corrected HAADF-STEM image (Fig. 1d). Furthermore, elemental mapping analysis in Fig. 1e validates the uniform distributions of C, N, O and Fe elements in Fe-N/O−C (MZ).

The composition of as made catalysts was characterized using X-ray photoelectron spectroscopy (XPS) and the results are listed in Table S1 and Table S2. The three peaks in Fig. S3 are corresponded to the C 1s (~284 eV), N 1s (~400 eV) and O 1s (~530 eV) [29]. The high-resolution N 1s in Fig. 2a was divided into five peaks assignable to pyridinic-N (~ 398.1 eV), Fe-N (~ 398.9 eV), pyrrolic-N (~ 400.2 eV), graphitic-N (~ 401.2 eV) and N-oxidized (~ 402.7 eV). [30] Additionally, high-resolution XPS O1 s spectra in Fig. S4 show a characteristic peak of Fe-O species at 530.7 eV [31,32]. For Fe-N/O-C (MZ), the contents of C, N and O are 92.52 at %, 2.93 at % and 4.55 at %, as determined by XPS analysis, while the content of Fe was determined to be 0.15 wt % by inductively coupled plasma optical emission spectroscopy (ICP-OES). Though all the samples contain pyridinic-N and Fe-N species, the Fe-N/O-C (MZ) has an absolute advantage in these two types of N, which are well known in facilitating CRR [33–36].

3.2. Fine structure of Fe-N/O-C (MZ)

To unravel the coordination structure of Fe atom in Fe-N/O−C (MZ), X-ray absorption spectroscopy (XAFS) measurements were carried out. In X-ray absorption near edge structure (XANES) spectra (Fig. 2b), the absorption edge position of Fe is located between those of Fe foil and FePC (II), indicating Fe manifests an intermediate valence between 0 and 2. As shown in Fig. 2c, the Fourier-transformed (FT) κ^3-weighted extended X-ray absorption fine structure (EXAFS) spectra of Fe-N/O−C (MZ) only exhibited a prominent peak at ~1.5 Å, which is attributed to the scattering peak of Fe-N-C first coordination shell. [37] Besides, no peeks of Fe-Fe bonds are found at 2.2 Å in EXAFS spectra, suggesting the Fe atoms are atomically dispersed [28]. Additionally, the data fittings in Fig. 2d reveal that the coordination number of Fe is around five with an average bond distance of 1.99 Å (Table S3). The wavelet transform (WT) results prompt the existence of Fe-O (maximum at 3.6 $Å^{-1}$) in the Fe-N/O−C (MZ) sample, situated between Fe-N and Fe-O in FePC (II) and Fe_2O_3 respectively [38,39]. Consequently, based on the EXAFS analysis, we put forward a reasonable Fe-N_xO_{5-x} structure for the coordinated Fe atoms in Fe-N/O−C (MZ) material. According to the peak quantification of XPS listed in Table S2, the atomic content of Fe-N and Fe-O are 0.55 at % and 0.14 at % respectively, which means the x in Fe-N_xO_{5-x} is almost equal to four. Inferred from above analysis, we put forward a reasonable Fe-N_4O structure as the new kind of active center for electrocatalytic CRR. Then, the structures of Fe-N_4O was further optimized by using DFT calculations and the configuration with the lowest free energy is selected, where four nitrogen atoms in-plane and one oxygen atom out-of-plane are coordinated to Fe atom, as illustrated in Fig. 2d.

3.3. BET surface and pore structures of Fe-N/O-C

Given the extremely importance of high surface area and pores distribution for the active site fixation and mass transfer, the hierarchical carbon framework structures of as-prepared catalysts were studied by N_2 adsorption-desorption measurements. The detail results of BET surface area and *t*-Plot micropore area derived from N_2 adsorption-desorption curve are listed in Table S4. The specific surface areas are 1173, 897, 667 $m^2\ g^{-1}$ for Fe-N/O-C (MZ), Fe-N/O-C (M) and Fe-N/O-C (Z), respectively. Notably, compared to the control samples, the BET surface area of Fe-N/O-C (MZ) was significantly enhanced due to the pore-formation function of MgO and $ZnCl_2$ as templates during carbonation process. Besides, the well-defined hysteresis loops at high-pressure region (P/P_0 = 0.5–1.0) in Fig. S5a suggest the coexistence of micro- and meso-pores for all the synthesized samples. Since the mesopores in the carbon framework have been proved in facilitating the adsorption of CO_2 [40], an essential step of CRR, it is necessary to reveal the specific roles of MgO and $ZnCl_2$ towards the mesoporous formation. In Fe-N/O-C (M), the content of micropores (46.7 %) and mesopores (53.3 %) are comparable, indicating MgO as template has equal effects to the formation of micro- and meso- pores. While in Fe-N/O-C (Z), the mesopores only accounts for 0.4 %, which indicates that $ZnCl_2$ as single template can only make micropores in the carbonation process. Surprisingly, by using MgO and $ZnCl_2$ as double templates, the percent of mesopores in Fe-N/O-C (MZ) is evaluated to 75.5 % dramatically, confirming $ZnCl_2$ can elevate the MgO and in constructing mesoporous during carbonation process. Furthermore, the SEM images (Fig. S6) visually shows the different morphology of carbon skeleton structure of the three Fe-N/O-C materials as made, confirming the outstanding micro- and meso- porous structures of Fe-N/O-C (MZ).

3.4. CRR activity

The CRR activities were determined by linear sweep voltammetry (LSV) in a CO_2-saturated 0.1 M $KHCO_3$ solution, as shown in Fig. 3a. It is worth noting that Fe-N/O-C (MZ) delivers the highest current density

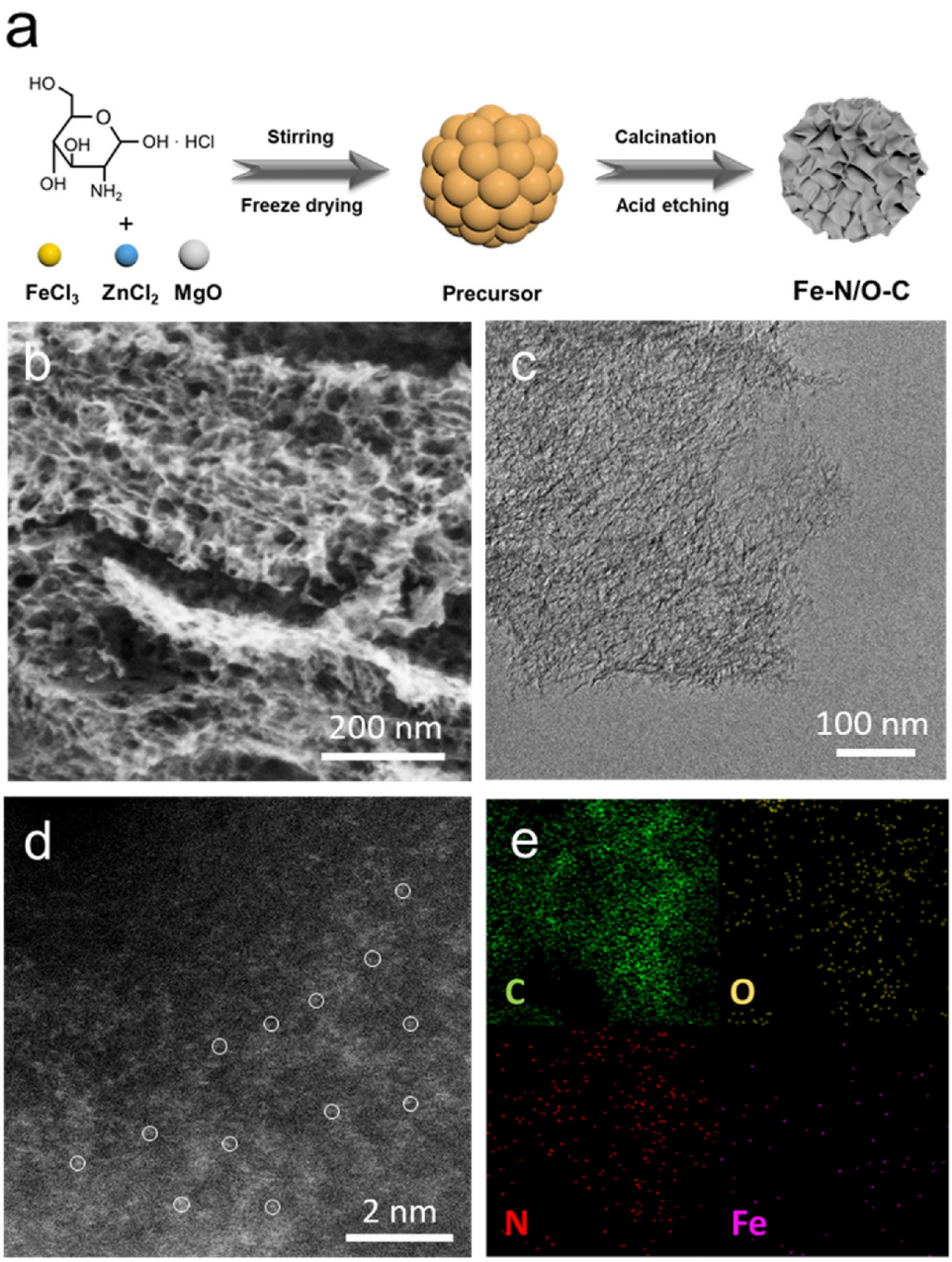

Fig. 1. (a) Schematic illustration, (b) SEM, (c) TEM, (d) Aberration-corrected HAADF-STEM of Fe single atoms (white circles), (e) EDS images of Fe-N/O-C (MZ) catalyst.

among all the three catalysts as made in the whole potential range tested, which is attributed to its large surface area, abundant mesoporous and high content of Fe-N_4O active sites. Controlled potential electrolysis was further performed at various potentials between -0.4 and -1.0 V vs RHE to confirm the CRR activities. The faradic efficiencies of all the products were recorded in Fig. 3b. It can be seen that carbon monoxide is the main product derived from CO_2 reduction while the only by-product detected in our gas products is H_2 on for all the catalysts. No liquid products is detected in ^{1}H NMR spectrum (Fig. S7). The highest selectivity for CO production reaches ~96 % at -0.57 V vs RHE (corresponding to a low overpotential of 460 mV) with the current density of -5.6 mA/cm^2 on Fe-N/O-C (MZ), while the TOF of CO normalized to Fe was calculated to 7820 h^{-1}. Besides, a comparison of the CO partial current densities on various catalysts (Fig. 3c) showing a monotonic increase with overpotential and following the order corresponding to their catalytic capacity, again underlining the excellent activity and selectivity of Fe-N/O-C (MZ) catalysts [41].

As control experiments, Fe-N/O-C (Z) only manifests a low FE of CO less than 40 % (Fig. 3b and Fig. S8) in the whole range of applied potentials, showing much poor catalytic performance than Fe-N/O-C (MZ). However, Fe-N/O-C (M) only behaved slightly lower FE of CO than that of Fe-N/O-C (MZ). As illustrated in Table S2, it can be concluded that the FE of CO is not always in line with the Fe-N or Fe-O content, indicating the activity and selectivity of CRR are not only determined by the population of Fe-N_4O moieties, but also restricted to the hierarchical pores of carbon framework in the catalysts [42]. For the gas-involved electrochemical reactions in aqueous solution, the micropores in the catalysts is pivotal to the adsorption of gas while the mesopores are necessary for the mass transfer of solvated species [43]. With only $ZnCl_2$ as template, Fe-N/O-C (Z) has few mesopores, limiting the mass transfer of electrolyte to the actives sites associating with the lowest FE of CO among three catalysts as made. Both containing MgO template, the content of mesopores in Fe-N/O-C (M) is close to that of Fe-N/O-C (MZ), resulting an approximately catalytic performance with

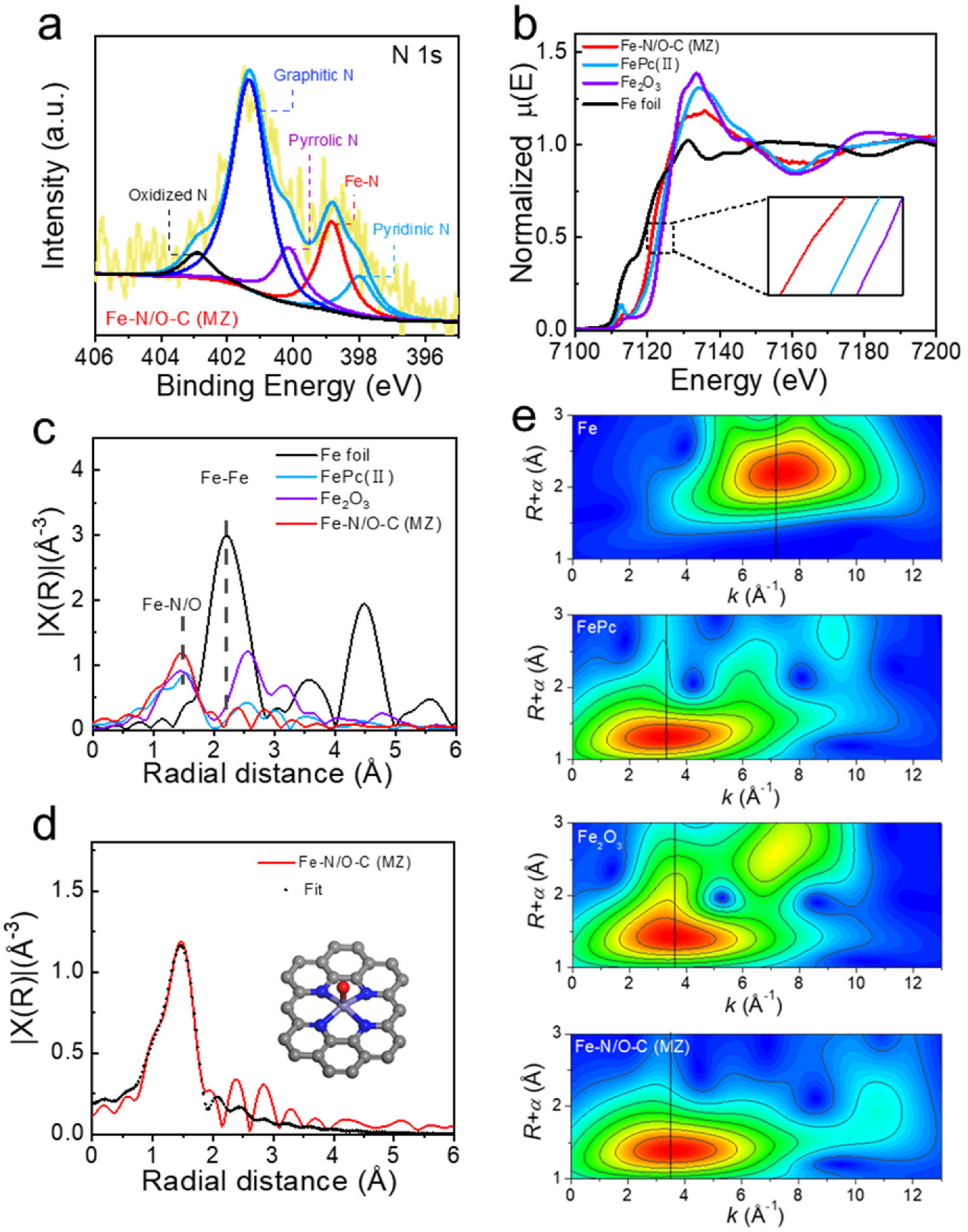

Fig. 2. (a) XPS N 1s spectra, (b) Normalized Fe K-edge XANES spectra, (c) Fourier-transform EXAFS spectrums, (d) EXAFS spectra fitting curves and schematic model of Fe-N/O-C (MZ): Fe (purple), O (red), N (blue), and C (gray), (e)WT of Fe foil, FePC (II), Fe_2O_3 and Fe-N/O-C (MZ) (from top to bottom).(For interpretation of the references to color in the Figure, the reader is referred to the web version of this article).

Fe-N/O-C (MZ). However, without $ZnCl_2$ as template, the Fe-N/O-C (M) manifests a slightly lower activity than Fe-N/O-C (MZ), confirming the key role of micropores in carbon dioxide adsorption. All the results proved that apart from the metal active sites, the well-designed pore structure also plays a key role in determining the catalytic performance of M-N-C materials for CRR. Besides, it is a promising strategy for constructing mesoporous carbon frameworks by using two templates.

The catalytic durability of Fe-N/O-C (MZ) was performed by a long-term CO_2 electrocatalysis at -0.57 V vs RHE. Noteworthy, the total current density maintains a steady value of -5.6 ~ -6.1 mA cm^{-2} and the faradic efficiency of CO is retained at 95 ~ 96 % throughout the 22 h electrolysis. We also compared the catalytic performance of our electrocatalysts with other Fe-N-C catalysts reported elsewhere (Table S5). Results show that our Fe-N/O-C (MZ) catalyst gives a relatively high activity and selectivity. More importantly, when the applied potential exceeds the optimum one, the FE of CO only has a much weaker attenuation on Fe-N/O-C (MZ) compared to other Fe-N-C catalysts, as shown in Fig. 3b. This is desirable for the industrial application, especially when high current density and advanced selectivity are both acquired at the same time.

3.5. Density functional theory (DFT) calculations and CRR mechanism

To investigate the origin of high catalytic performance of Fe-N/O-C (MZ) for CRR, the DFT calculations are performed to investigate the catalytic mechanism of Fe-N_4O center for CRR to CO, while the Fe-N_4 and Fe-N_5 structures were also studied as comparison. It is generally accepted that the electroreduction of CO_2 to CO on metal active sites include three elementary steps, the initial state (CO_2 molecule), adsorbed intermediate states (*COOH, *CO) and terminal state (CO molecule) [23,44,45]. The free energy of *COOH usually reflects the CRR activity in view of the limiting overpotential. In addition, the desorption of *CO will affect the selectivity considerably by competing with HER [46]. It can be seen in Fig. 4b that the Fe-N_4 structure could reduce

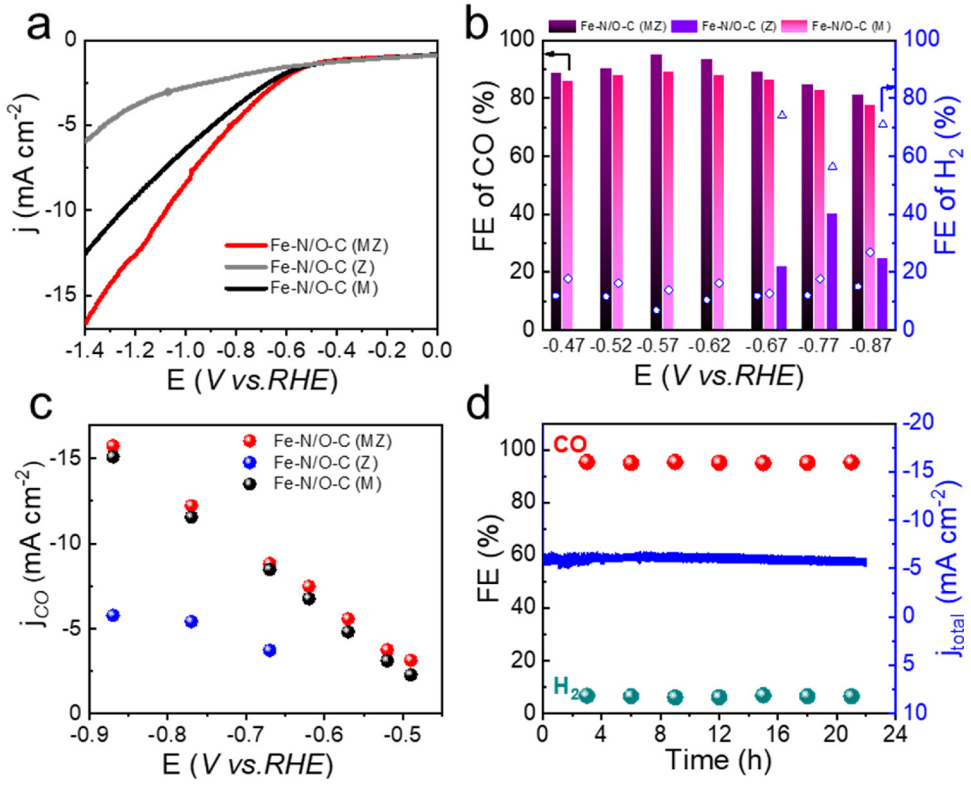

Fig. 3. (a) LSV curves, (b) FE of CO and H_2, (c) CO current densities, (d) Chronoamperograms (blue line) and FE_{CO} (red ball) at -0.57 V vs RHE. (For interpretation of the references to color in the Figure, the reader is referred to the web version of this article).

CO_2 to *COOH with an exothermic energy of 0.05 eV. However, the desorption of *CO to CO needs to overcome a high endothermic energy barrier of 1.74 eV, which makes it the rate determining step (RDS) of CO_2-to−CO. Meanwhile, the RDS of HER on Fe-N_4 site is the desorption of *H to H_2, which has a much more endothermic energy of 2.99 eV (Fig. S9). When the applied potentials exceed the optimal one, the RDS of CRR and HER speed up simultaneously while the later one rises more significantly due to its larger activation energy. Therefore, the FE of CO drop quickly under the higher negative potentials because of the acceleration of HER.

Surprisingly, for the Fe-N_4O site, the CO adsorption strength is greatly reduced, favoring the desorption of *CO to CO thermodynamically under the experimental conditions. The RDS of CO_2-to−CO on Fe-N_4O changes the reduction of CO_2 to *COOH. Different rate determining step suggests that Fe-N_4O unit has an absolute advantage at high overpotential. Moreover, hydrogen adsorption was also considered in Fig. S9. Dramatically, the Fe-N_4O shows much higher formation energy for H* adsorption (1.29 eV) than that of Fe-N_4 (-2.99 eV), proving that the HER is well inhibited on Fe-N_4O even under higher overpotentials. So far, we can understand why the Fe-N_4O-C catalyst maintains a high selectivity towards CO over a wide potential range from -0.47 to -0.87 V vs RHE. Similar with Fe-N_4O, it can be seen that the RDS of CO_2-to−CO on Fe-N_5 is also the formation of *COOH but with a higher energy barrier (1.98 eV) compared to that of Fe-N_4O (1.48 eV). Therefore, it is predicted that Fe-N_4O have a better intrinsic activity than Fe-N_5 as electrocatalysts for CRR.

4. Conclusion

In conclusion, a hierarchically micro- and meso-porous Fe-N_4O-doped carbon material has been prepared via simple one-step pyrolysis and acid leaching method. Used as electrocatalyst for CRR, an exceptionally outstanding catalytic performance with high faradic efficiency (~96 %) of CO and improved current density (-5.4 mA cm^{-2})

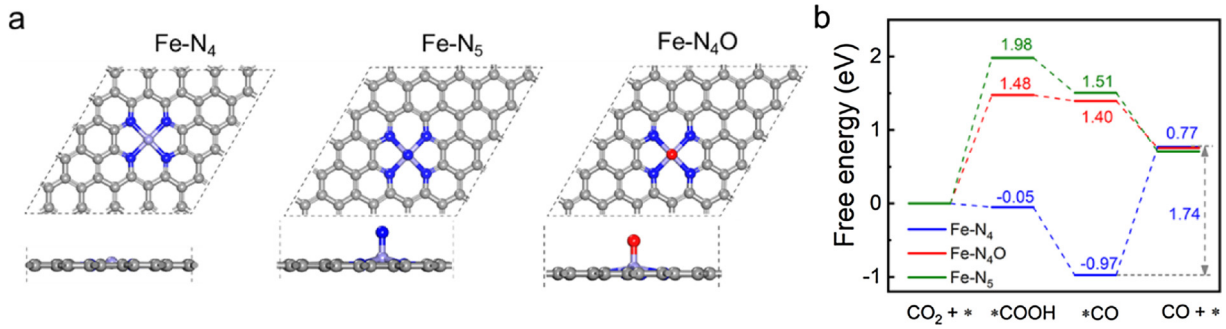

Fig. 4. (a) Top and side views of the relaxed Fe-N_4, Fe-N_5 and Fe-N_4O configurations. The gray, blue, purple, and red balls represent C, N, Fe, and O atoms, respectively. (b) Calculated free energy evolution of CO_2 reduction to CO on Fe-N_4, Fe-N_5 and Fe-N_4O under an applied electrode potential of 0 V. (For interpretation of the references to color in the Figure, the reader is referred to the web version of this article).

codoped

were achieved, together with a low potential of 470 mV and excellent stability. Experiments and DFT calculations illuminate the key role of Fe-N_4O structure in favoring the desorption of *CO and inhibiting the adsorption of H* on Fe atom, leading to the excellent selectivity for CO_2-to−CO in a wide electrochemical window. Besides, the mesoporous structure of carbon framework derived from the synergistic template effects of MgO and $ZnCl_2$ further elevates the activity of Fe-N_4O site. This work suggests a new strategy for designing M-N-C materials as highly efficient and durable electrocatalysts for CRR.

CRediT authorship contribution statement

Xiaoshan Wang: Conceptualization, Methodology, Writing - original draft. **Yuanyuan Pan:** Software. **Hui Ning:** Writing - review & editing, Supervision. **Hongmei Wang:** Methodology. **Dianliang Guo:** Validation. **Wenhang Wang:** Formal analysis. **Zhongxue Yang:** Investigation. **Qingshan Zhao:** Data curation. **Bingxing Zhang:** Formal analysis. **Lirong Zheng:** Data curation. **Jianling Zhang:** Writing - review & editing. **Mingbo Wu:** Supervision.

Declaration of Competing Interest

The authors declare that they have no known competing financial interests or personal relationships that could have appeared to influence the work reported in this paper.

Acknowledgements

This work is financially supported by the National Natural Science Foundation of China (21808242); the Shandong Provincial Natural Science Foundation (ZR2018BB070, ZR2018ZC1458); the Fundamental Research Funds for the Central Universities of China (19CX02042A).

Appendix A. Supplementary data

Supplementary material related to this article can be found, in the online version, at doi:https://doi.org/10.1016/j.apcatb.2020.118630.

References

[1] Y.L. Yang, M.G. Wu, X.W. Zhu, H. Xu, S. Ma, Y.F. Zhi, H. Xia, X.M. Liu, J.Y. Tang, S.P. Chai, L. Palmisano, F. Parrino, J.M. Ma, 2020 Roadmap on two-dimensional nanomaterials for environmental Catalysis, Chin. Chem. Lett. 30 (2019) 2065–2088, https://doi.org/10.1016/j.cclet.2019.11.001.

[2] Y.L. Yang, Y. Tang, H.M. Jiang, Y.M. Chen, P.Y. Wan, M.H. Fan, R.R. Zhang, S. Ullan, L. Pan, J.M. Ma, 2020 Roadmap on gas-involved photo- and electro- catalysis, Chin. Chem. Lett. 30 (2019) 2089–2109, https://doi.org/10.1016/j.cclet.2019.10.041.

[3] M.G. Wu, B.L. Xu, Y.F. Zhang, S.H. Qi, W. Ni, J. Hu, J.M. Ma, Perspectives in emerging bismuth electrochemistry, Chem. Eng. J. 381 (2020) 122558, , https://doi.org/10.1016/j.cej.2019.122558.

[4] J. Ma, Y. Zhang, Y. Zhao, Z. Wei, J. Yang, C. Wang, Phys. Zn-Doped Cu(100) facet with efficient catalytic ability for the CO_2 electroreduction to ethylene, Chem. Chem. Phys. 21 (2019) 21341–21348, https://doi.org/10.1039/C9CP03692J.

[5] B.X. Zhang, J.L. Zhang, J.B. Shi, D.X. Tan, L.F. Liu, F.Y. Zhang, C. Lu, Z.Z. Su, X.N. Tan, X.Y. Cheng, B.X. Han, L.R. Zheng, J. Zhang, Manganese acting as a high-performance heterogeneous electrocatalyst in carbon dioxide reduction, Nat. Commun. 10 (2019) 2980, https://doi.org/10.1038/s41467-019-10854-1.

[6] N. Leonard, W. Ju, I. Sinev, J. Steinberg, F. Luo, A.S. Varela, The chemical identity, state and structure of catalytically active centers during the electrochemical CO_2 reduction on porous Fe-nitrogen-carbon (Fe-N-C) materials, Chem. Sci. 9 (2018) 5064–5073, https://doi.org/10.1039/C8SC00491A.

[7] C.C. Yan, H.L. Li, Y.F. Ye, H.H. Wu, F. Cai, R. Si, J.P. Xiao, S. Miao, S.H. Xie, F. Yang, Y.S. Li, G.X. Wang, X.H. Bao, Coordinatively unsaturated nickel–nitrogen sites towards selective and high-rate CO_2 electroreduction, Energy Environ. Sci. 11 (2018) 1204–1210, https://doi.org/10.1039/c8ee00133b.

[8] M.L. Zhang, T.-S. Wu, S. Hong, Q. Fan, Y.-L. Soo, J. Masa, J.S. Qiu, Z.Y. Sun, Efficient electrochemical reduction of CO_2 by Ni–N catalysts with tunable performance, ACS Sustainable Chem. Eng. 7 (2019) 15030–15035, https://doi.org/10.1021/acssuschemeng.9b03502.

[9] H.J. Yang, J. Dong, Y.H. Hong, W.F. Lin, Z.Y. Zhou, S.G. Sun, Comparative investigation of CO_2 and oxygen reduction on Fe/N/C catalysts, Electrochem. commun. 97 (2018) 82–86, https://doi.org/10.1016/j.elecom.2018.10.014.

[10] Q.Q. Cheng, K. Mao, L.S. Ma, L.J. Yang, L.L. Zou, Z.Q. Zou, Z. Hu, H. Yang, Encapsulation of iron nitride by Fe-N-C shell enabling highly efficient electroreduction of CO_2 to CO, ACS Energy Lett. 3 (2018) 1205–1211, https://doi.org/10.1021/acsenergylett.8b00474.

[11] C. Hu, S.L. Bai, L.J. Gao, S.C. Liang, J. Yang, S.-D. Cheng, S.-B. Mi, J.S. Qiu, Porosity-induced high selectivity for CO_2 electroreduction to CO on Fe-doped ZIF-derived carbon catalysts, ACS Catal. 9 (2019) 11579–11588, https://doi.org/10.1021/acscatal.9b03175.

[12] A.S. Varela, W. Ju, P. Strasser, Molecular nitrogen-carbon catalysts, solid metal organic framework catalysts, and solid Metal/Nitrogen-Doped carbon (MNC) catalysts for the electrochemical CO_2 reduction, Adv. Energy Mater. 8 (2018) 1703614, , https://doi.org/10.1002/aenm.201703614.

[13] W. Ju, A. Bagger, G.P. Hao, A.S. Varela1, I. Sinev, V. Bon, B.R. Cuenya, S. Kaskel, J. Rossmeisl, P. Strasser, Understanding activity and selectivity of metal-nitrogen-doped carbon catalysts for electrochemical reduction of CO_2, Nat. Commun. 8 (2017) 944, https://doi.org/10.1038/s41467-017-01035-z.

[14] F.P. Pan, H.G. Zhang, K.X. Liu, D. Cullen, K. More, M.Y. Wang, Z.X. Feng, G.F. Wang, G. Wu, Y. Li, Unveiling active sites of CO_2 reduction on nitrogen-coordinated and atomically dispersed Iron and cobalt catalysts, ACS Catal. 8 (2018) 3116–3122, https://doi.org/10.1021/acscatal.8b00398.

[15] S.Q. Zhu, Q. Wang, X.P. Qin, M. Gu, R. Tao, B.P. Lee, L.L. Zhang, Y.Z. Yao, T.H. Li, M.H. Shao, Tuning structural and compositional effects in Pd-Au nanowires for highly selective and active CO_2 electrochemical reduction reaction, Adv. Energy Mater. (2018) 1802238, https://doi.org/10.1002/aenm.201802238.

[16] T.N. Huan, N. Ranjbar, G. Rousse, M. Sougrati, A. Zitolo, V. Mougel, F. Jaouen, M. Fontecave, Electrochemical reduction of CO_2 catalyzed by Fe-N-C materials: a structure-selectivity study, ACS Catal. 7 (2017) 1520–1525, https://doi.org/10.1021/acscatal.6b03353.

[17] M.B. Ross, P.D. Luna, Y.F. Li, C.T. Dinh, D. Kim, P.D. Yang, E.H. Sargent, Designing materials for electrochemical carbon dioxide recycling, Nat. Catal. 2 (2019) 648–658, https://doi.org/10.1038/s41929-019-0306-7.

[18] S. Back, J. Lim, N.Y. Kim, Y.H. Kim, Y. Jung, Single-atom catalysts for CO_2 electroreduction with significant activity and selectivity improvements, Chem. Sci. 8 (2017) 1090–1096, https://doi.org/10.1039/C6SC03911A.

[19] W.H. Ren, X. Tan, W.F. Yang, C. Jia, S.M. Xu, K.X. Wang, S.C. Simith, C. Zhao, Isolated diatomic Ni-Fe metal-nitrogen sites for synergistic electroreduction of CO_2, Angew. Chem. Int. Ed. 58 (2019) 6972–6976, https://doi.org/10.1002/anie.201901575.

[20] H.N. Zhang, J. Li, S.B. Xi, Y.H. Du, X. Hai, J.Y. Wang, H.M. Xu, J. Zhang, J. Lu, J. Z. Graphene supported single-atom FeN_5 catalytic site for efficient electrochemical CO_2 reduction, Angew. Chem. Int. Ed. 131 (2019) 15013–150018, https://doi.org/10.1002/ange.201906079.

[21] F.P. Pan, W. Deng, C. Justiniano, Y. Li, Identification of champion transition metals centers in metal and nitrogen-codoped carbon catalysts for CO_2 reduction, Appl. Catal. B: Environ. 226 (2018) 463–472, https://doi.org/10.1016/j.apcatb.2018.01.001.

[22] H.Q. Li, N. Xiao, M.Y. Hao, X.D. Song, Y.W. Wang, Y.Q. Ji, C. Liu, C. Li, Z. Guo, F. Zhang, J.S. Qiu, Efficient CO_2 electroreduction over pyridinic-N active sites highly exposed on wrinkled porous carbon nanosheets, Chem. Eng. J. 351 (2018) 613–621, https://doi.org/10.1016/j.cej.2018.06.077.

[23] X.C. Duan, J.T. Xu, Z.X. Wei, J.M. Ma, S.J. Guo, S.Y. Wang, H.K. Liu, S.X. Dou, Metal-free carbon materials for CO_2 electrochemical reduction, Adv. Mater. 29 (2017) 1701784, , https://doi.org/10.1002/adma.201701784.

[24] H. Wang, J. Jia, P.F. Song, Q. Wang, D.B. Li, S.X. Min, C.X. Qian, L. Wang, Y.F. Li, C. Ma, T. Wu, J.Y. Yuan, M. Antonietti, G.A. Ozin, Efficient Electrocatalytic Reduction of $CO_2$by Nitrogen-Doped Nanoporous Carbon/Carbon Nanotube Membranes - A Step Towards the Electrochemical CO_2 Refinery, Angew. Chem. Int. Ed. 56 (2017) 7847–7852, https://doi.org/10.1002/ange.201703720.

[25] F.A.C. Pastrián, A.G.M. da Silva, A.H.B. Dourado, A.P. de Lima Batista, A.G.S. de Oliveira-Filho, J. Quiroz, D.C. de Oliveira, P.H.C. Camargo, S.I.C. de Torresi, Why could the nature of surface facets lead to differences in the activity and stability of Cu_2O-Based electrocatalytic sensors? ACS Catal. 8 (2018) 6265–6272, https://doi.org/10.1021/acscatal.8b00726.

[26] C.W. Lee, J.S. Hong, K.D. Yang, K. Jin, J.H. Lee, H.Y. Ahn, H.M. Seo, N.E. Sung, K.T. Nam, Selective electrochemical production of formate from Carbon Dioxide with bismuth-based catalysts in an aqueous electrolyte, ACS Catal. 8 (2018) 931–937, https://doi.org/10.1021/acscatal.7b03242.

[27] X.L. Zu, X.D. Li, W. Liu, Y.F. Sun, J.Q. Xu, T. Yao, W.S. Yan, S. Gao, C.M. Wang, S.Q. Wei, Y. Xie, Efficient and Robust Carbon Dioxide Electroreduction Enabled by Atomically Dispersed $Sn\delta^+$ Sites, Adv. Mater. 3 (2019) 1808135, , https://doi.org/10.1002/adma.201808135.

[28] C.J. Lei, H.Q. Chen, J.H. Cao, J. Yang, M. Qiu, Y. Xia, C. Yuan, B. Yang, Z.J. Li, X.W. Zhang, L.C. Lei, J. Abbott, Y. Zhong, X.H. Xia, G. Wu, Q.G. He, Y. Hou, Fe-N_4 sites embedded into carbon nanofiber integrated with electrochemically exfoliated graphene for oxygen evolution in acidic medium, Adv. Energy Mater. 8 (2018) 1801912, , https://doi.org/10.1002/aenm.201801912.

[29] H. Ning, X.S. Wang, W.H. Wang, Q.H. Mao, Z.H. Yang, Q.S. Zhao, Y. Song, M.B. Wu, Cubic Cu_2O on nitrogen-doped carbon shell for electrocatalytic CO_2 reduction to C_2H_4, Carbon 146 (2019) 218–223, https://doi.org/10.1016/j.carbon.2019.02.010.

[30] Y. Guo, H.J. Yang, X. Zhou, K.L. Liu, C. Zhang, Z.Y. Zhou, C. Wang, W.B. Lin, Electrocatalytic reduction of CO_2 to CO with 100% faradaic efficiency by using pyrolyzed zeolitic imidazolate frameworks supported on carbon nanotube networks, J. Mater. Chem. A. 5 (2017) 24867–24873, https://doi.org/10.1039/C7TA08431E.

[31] S.S. Su, Y.Y. Liu, X.M. Liu, W. Jin, Y.P. Zhao, Transformation pathway and degradation mechanism of methylene blue through β-FeOOH@GO catalyzed photo-

Fenton-like system, Chemosphere 218 (2019) 83–92, https://doi.org/10.1016/j.chemosphere.2018.11.098.
[32] Y.S. Luo, J.S. Luo, J. Jiang, W.W. Zhou, H.P. Yang, X.Y. Qi, H. Zhang, H.J. Fan, D.Y.W. Yu, C.M. Li, T. Yu, Seed-assisted synthesis of highly ordered TiO_2@α-Fe_2O_3 core/shell arrays on carbon textiles for lithium-ion battery applications, Energy Environ. Sci. 5 (2012) 6559, https://doi.org/10.1039/c2ee03396h.
[33] J.J. Wu, M.J. Liu, P.P. Sharma, R.M. Yadav, L.L. Ma, Y.C. Yang, X.L. Zou, X.D. Zhou, R. Vajtai, B.I. Yakobson, J. Lou, P.M. Ajayan, Incorporation of nitrogen defects for efficient reduction of CO_2 via Two-Electron Pathway on three-dimensional graphene foam, Nano Lett. 16 (2016) 466–470, https://doi.org/10.1021/acs.nanolett.5b04123.
[34] X.T. Meng, C. Yu, X.D. Song, Y. Liu, S.X. Liang, Z.Q. Liu, C. Hao, J.S. Qiu, Nitrogen-doped graphene nanoribbons with surface enriched active sites and enhanced performance for dye-sensitized solar cells, Adv. Energy Mater. 5 (2015) 1500180, , https://doi.org/10.1002/aenm.201500180.
[35] H.Q. Li, N. Xiao, Y.W. Wang, C. Li, X. Ye, Z. Guo, X. Pan, C. Liu, J.P. Bai, J. Xiao, X.Y. Zhang, S.J. Zhao, J.S. Qiu, Nitrogen-doped tubular carbon foam electrodes for efficient electroreduction of CO_2 to syngas with potential-independent CO/H_2 ratios, J. Mater. Chem. A 7 (2019) 18852–18860, https://doi.org/10.1039/c9ta05904k.
[36] C. Li, Y.W. Wang, N. Xiao, H.Q. Li, Y.Q. Ji, Z. Guo, C. Liu, J.S. Qiu, Nitrogen-doped porous carbon from coal for high efficiency CO_2 electrocatalytic reduction, Carbon 151 (2019) 46–52, https://doi.org/10.1016/j.carbon.2019.05.042.
[37] Y.R. Xue, B.L. Huang, Y.P. Yi, Y. Guo, Z.C. Zuo, Y.J. Li, Anchoring zero valence single atoms of nickel and iron on graphdiyne for hydrogen evolution, Nat. Commun. 9 (2018) 1460, https://doi.org/10.1038/s41467-018-03896-4.
[38] Y.J. Chen, S.F. Ji, Y.G. Wang, J.C. Dong, W.X. Chen, Z. Li, R.G. Shen, L.R. Zheng, Z.B. Zhuang, D.S. Wang, Y.D. Li, Isolated single Iron atoms anchored on N-Doped porous carbon as an efficient electrocatalyst for the oxygen reduction reaction, Angew. Chem. Int. Ed. 56 (2017) 6937–6941, https://doi.org/10.1002/ange.201702473.
[39] Y.C. Lin, P.Y. Liu, E. Velasco, G. Yao, Z.Q. Tian, L.J. Zhang, L. Chen, Fabricating single-atom catalysts from chelating metal in open frameworks, Adv. Mater. 31 (2019) 1808193, , https://doi.org/10.1002/adma.201808193.
[40] J. Wei, D.D. Zhou, Z.K. Sun, Y.H. Deng, Y.Y. Xia, D.Y. Zhao, Controllable synthesis of rich nitrogen-doped ordered mesoporous carbon for CO_2 capture and supercapacitors, Adv. Funct. Mater. 23 (2013) 2322–2328, https://doi.org/10.1002/adfm.201202764.
[41] A.S. Varela, N.R. Sahraie, J. Steinberg, W. Ju, H.S. Oh, P. Strasser, Metal-doped nitrogenated carbon as an efficient catalyst for direct CO_2 electroreduction to CO and hydrocarbons, Angew. Chem. Int. Ed. 54 (2015) 10758–10762, https://doi.org/10.1002/ange.201502099.
[42] C.H. Zhang, S.Z. Yang, J.J. Wu, M.J. Liu, S. Yazdi, M.Q. Ren, J.W. Sha, J. Zhong, K.Q. Nie, A.S. Jalilov, Z.Y. Li, H.M. Li, B.I. Yakobson, Q. Wu, E. Ringe, H. Xu, P.M. Ajayan, J.M. Tour, Electrochemical CO_2 reduction with atomic iron-dispersed on nitrogen-doped graphene, Adv. Energy Mater. 8 (2018) 1703487, , https://doi.org/10.1002/aenm.201703487.
[43] R. Zhao, Z.B. Liang, S. Gao, C. Yang, B.J. Zhu, J.L. Zhao, C. Qu, R.Q. Zou, Q. Xu, Puffing up energetic metal-organic frameworks to large carbon networks with hierarchical porosity and atomically dispersed metal sites, Angew. Chem. Int. Ed. 58 (2019) 1975–1979, https://doi.org/10.1002/ange.201811126.
[44] W.L. Zhu, Y.-J. Zhang, H.Y. Zhang, H.F. Lv, Q. Li, R. Michalsky, A.A. Peterson, S.H. Sun, Active and selective conversion of CO_2 to CO on ultrathin Au nanowires, J. Am. Chem. Soc. 136 (2014) 16132–16135, https://doi.org/10.1021/ja5095099.
[45] X.M. Hu, H.H. Hval, E.T. Bjerglund, K.J. Dalgaard, M.R. Madsen, M.M. Pohl, E. Welter, P. Lamagni, K.B. Buhl, M. Bremholm, M. Beller, S.U. Pedersen, T. Skrydstrup, K. Daasbjerg, Selective CO_2 reduction to CO in water using earth-abundant metal and nitrogen-doped carbon electrocatalysts, ACS Catal. 8 (2018) 6255–6264, https://doi.org/10.1021/acscatal.8b01022.
[46] H.B. Yang, S.F. Hung, S. Liu, K.D. Yuan, S. Miao, L.P. Zhang, X. Huang, H.Y. Wang, W.Z. Cai, R. Chen, J.J. Gao, X.F. Yang, W. Chen, Y.Q. Huang, H.M. Chen, C.M. Li, T. Zhang, B. Liu, Atomically dispersed Ni(I) as the active site for electrochemical CO_2 reduction, Nat. Energy 3 (2018) 140–147, https://doi.org/10.1038/s41560-017-0078-8.